npj | imaging

Article

https://doi.org/10.1038/s44303-024-00051-1

Impact of dietary zinc on stimulated zinc secretion MRI in the healthy and malignant mouse prostate

Veronica Clavijo Jordan[1,2] ✉, André F. Martins[3,4,5], Erica Dao[6], Kalotina Geraki[7], Sara Chirayil[8], Xiaodong Wen[8], Pooyan Khalighinejad[8], Daniel Parrott[8], Xiaojing Wang[8], Patricia Gonzalez Pagan[1], Neil Rofsky[9], Michael Farquharson[10] & A. Dean Sherry[8,11,12]

Previous studies have shown that the zinc-responsive MRI probe, GdL1, can distinguish healthy versus malignant prostate tissues based upon differences in zinc content and secretion. In this study, mice were fed chow containing low, normal, or high zinc content for 3 weeks before imaging glucose stimulated zinc secretion (GSZS) by MRI. The distribution of zinc in prostate tissue in these three groups was imaged by synchrotron radiation X-ray fluorescence (SR-XRF). A zinc deficiency caused systemic and organ-level dysregulation, weight loss, and altered zinc bioavailability. Zinc efflux from the prostate increased in parallel to dietary zinc in healthy mice but not in TRAMP mice, consistent with a lowered capacity to store dietary zinc in malignant cells. This differential zinc efflux suggests that a dietary supplement of zinc prior to a GSZS study may enhance image contrast between healthy and malignant prostate tissue, thereby improving the accuracy of prostate cancer detection in man.

Divalent zinc (Zn^{2+}) is an essential trace element that plays many important roles in biology including a direct catalytic role in several metalloenzymes and a structural role in hundreds of zinc finger transcription factors[1]. Such catalytic and structural proteins have a high affinity for Zn^{2+} with K_d values in the range, 10^{-12} to 10^{-15} M[2]. Zn^{2+} ions also regulate the immune system modulating cell redox by interacting with dozens of different thiol-rich metallothionein proteins[3] and in cell-cell communication, cell proliferation, differentiation, and survival[4]. These physiological-type functions typically involve lower affinity Zn-protein and Zn-small molecule interactions that are kinetically very dynamic and primarily controlled by "freely" available Zn^{2+} in a cell. The amount of Zn^{2+} available for these cellular activities is regulated by several Zn^{2+} transporter proteins that either export Zn^{2+} out of cells or into subcellular compartments or vesicles to reduce freely available cytosolic Zn^{2+} (the ZnT family) or import Zn^{2+} into cells or out of subcellular vesicles to increase the amount of free Zn^{2+} in the cytosol (the Zip family)[5–7]. Thus, the amount of freely available Zn^{2+} in the cytosol of cells is largely controlled by the location and activity of these transporters[7]. One of the best known and widely studied transporters, ZnT8, imports Zn^{2+} from the cytosol of β-cells into vesicles for storage with insulin. It is thought that Zn^{2+} aids in crystallization of insulin so that more can be packaged into small-sized granules which can easily migrate to the cell surface for exocytosis[8]. Upon secretion of insulin in response to an increase in plasma glucose, the weakly bound Zn^{2+} ions are also released and the excess Zn^{2+} surrounding β-cells can be detected using optical dyes[9–11] or, as demonstrated recently, by use of a Zn-responsive MRI contrast agent in vivo[12–15]. Imaging glucose-stimulated zinc secretion (GSZS) from the in vivo pancreas by MRI not only detects individual islets in the intact pancreas but also distinguishes between islets that respond immediately to an increase in glucose (rapidly responding islets) from those that release insulin more slowly[14].

Imaging GSZS from the mouse pancreas by MRI led to the unexpected finding that Zn^{2+} is also secreted from the mouse prostate in response to a

---

[1]Athinoula A. Martinos Center for Biomedical Imaging, Department of Radiology, Massachusetts General Hospital, Harvard Medical School, Charlestown, MA, USA. [2]Institute for Innovation in Imaging (i3), Massachusetts General Hospital, Harvard Medical School, Boston, MA, USA. [3]Werner Siemens Imaging Center, Eberhard Karls University Tübingen, Tübingen, 72076, Germany. [4]Cluster of Excellence iFIT (EXC 2180) "Image-Guided and Functionally Instructed Tumor Therapies, " Eberhard Karls University Tübingen, Tübingen, Germany. [5]German Cancer Consortium (DKTK), partner site Tübingen German Cancer Research Center (DKFZ), Im Neuenheimer Feld 280, Heidelberg, 69120, Germany. [6]Department of Physics and Astronomy, McMaster University, Hamilton, ON, L8S 4K1, Canada. [7]Diamond Light Source, Harwell, Didcot, OX11 0DE, United Kingdom. [8]Advanced Imaging Research Center and Department of Radiology, University of Texas Southwestern Medical Center, Dallas, TX, USA. [9]Department of Diagnostic, Molecular, and Interventional Radiology, Icahn School of Medicine at Mount Sinai, New York City, NY, USA. [10]School of Interdisciplinary Science, McMaster University, Hamilton, ON, L8S 4K1, Canada. [11]Department of Chemistry, University of Texas at Dallas, Richardson, TX, USA. [12]VitalQuan, LLC, Dallas, TX, USA. ✉e-mail: mclavijojordan@mgh.harvard.edu

sudden increase in plasma glucose[16]. It is well-known that the human prostate contains more total Zn^{2+} than any other tissue in man and that Zn^{2+} levels drop significantly in malignant prostate tissues (see reviews[17–19]). This raised the question of whether imaging Zn^{2+} secretion (GSZS) by MRI might reflect differences in Zn^{2+} content in healthy *versus* malignant prostate tissue. Indeed, hypointense foci (reflecting a lack of Zn^{2+} secretion) were detected in prostate images of TRAMP mice[16] and in older male dogs with enlarged prostates (BPH)[20]. A further study of zinc content in mouse prostate as measured by synchrotron radiation X-ray fluorescence (SR-XRF) showed that glucose stimulates movement of Zn^{2+} from the glandular lumen to the stromal and interstitial spaces where it comes into contact with the Zn-responsive MR contrast agent[21]. Although the mechanism by which glucose triggers Zn^{2+} secretion has not been fully delineated, a recent study in human immortalized prostate epithelial cells, PNT1A, showed that exposure of cells to high glucose initiated rearrangement of zinc transporters that resulted in net export of Zn^{2+} from cells via ZnT1 and an increase in lysosomal storage of Zn^{2+} via ZnT4 transporters[22]. Further comparative experiments in PNT1A cells *versus* the in vivo mouse prostate using various inhibitors and secretagogues have shown that glycolytic flux is necessary to initiate GSZS in vivo[23].

Given that the dietary zinc intake can be variable amongst men, the motivation and novelty of the current study was to examine the impact of altered dietary Zn^{2+} on 1) total zinc content in prostate tissues (by SR-XRF) and on 2) glucose-stimulated zinc secretion (by MRI) in healthy control mice and in TRAMP (transgenic adenocarcinoma of the mouse prostate) mice. TRAMP mice, a common model in studies of prostate cancer (PCa), spontaneously develop cancer a few weeks after birth[21]. After 3 weeks of controlled feeding, MR images of the prostate were collected before and after i.p. injection of glucose to stimulate zinc secretion. After collection of multiple MR images over 10 min, each animal was sacrificed at 10 min after injection of glucose, the prostate was quickly removed and frozen, and blood was collected for analysis. The frozen tissues were later sliced, mounted, and prepared for SR-XRF analyses. The data show only minor differences in total Zn^{2+} content in prostate tissue in animals fed chow containing 0.05 ppm, 30 ppm, or 150 ppm total zinc over 3 weeks while Zn^{2+} efflux as measured by GSZS MRI increased significantly in healthy animals in proportion to the amount of dietary Zn^{2+} but not in TRAMP animals. These combined results show that the zinc content of prostate tissue is not impacted significantly by dietary Zn^{2+} but that Zn^{2+} is more readily released from healthy prostate epithelial cells than malignant cells in response to increased plasma glucose. These results suggest that a dietary supplement of Zn^{2+} prior to a GSZS study in men may augment image contrast between healthy and malignant prostate tissue and thus facilitate prostate cancer detection by MRI.

Results

Study design and physiological effects of altered dietary zinc on metabolism and mineral bioavailability

In this study, we used a combination of molecular magnetic resonance imaging (MRI) and synchrotron radiation X-ray fluorescence (SR-XRF) imaging to interrogate the systemic and prostatic adaptations to dietary alterations in zinc content. Here, wildtype (WT) and transgenic adenocarcinoma of the mouse prostate (TRAMP) mice were fed either a zinc deficient (0.05 ppm), sufficient (30 ppm), or supplemented (150 ppm) diet for 21 days prior to imaging. Animals (16 weeks and 24 weeks of age) were fasted overnight prior to imaging. GSZS was initiated by bolus injection of glucose in the presence of the zinc probe, GdL1, as described previously[13]. GdL1 binds with Zn^{2+} ions released from cells ($K_{DZn} = 118$ nM) and that binary complex then forms a ternary complex with albumin which is detected as an increase in T_1 relaxivity (r_1). Previous molecular modeling and binding studies showed that GdL1 binds at two different sites on albumin with Zn^{2+} acting as a bridge between GdL1 and albumin[13]. Fig. 1 illustrates the mechanism. Zinc-free GdL1 has a $r_1 = 5.1\ mM^{-1}s^{-1}$ (0.5 T) which increases to $r_1 = 11.4\ mM^{-1}s^{-1}$ in the presence of Zn^{2+} and albumin, a change that results in an increase in image intensity in T_1-weighted MR images. T_1-weighted MRI scans were obtained before and after i.v. injection of 0.06 mmol/kg GdL1 and i.p. injection of 2.2 mmol/kg glucose. Three MR images were collected serially over 10 min before each animal was euthanized and the prostate removed and frozen for later SR-XRF analyses. 10 µm tissue slices were mounted on glass slides for H&E, and an adjacent 50 µm slice was mounted on XRF-compatible film and holder, as shown in Fig. 1B. Blood samples were also collected for analytical measurement of Gd and Zn by ICP-MS.

Prior to imaging, each animal was weighed, and blood was collected via a tail vein puncture to measure blood glucose before and after administration of GdL1 and glucose. After euthanasia, whole blood was collected, and serum was separated by centrifugation. As shown in Fig. 2A, alterations in dietary Zn affected the median weight of healthy animals; animals on a zinc-deficient diet had a significantly lower median weight ($W_{0.05\ ppm} = 28.0 \pm 2.20$ g) compared to animals who received a zinc-sufficient diet ($W_{30\ ppm} = 30.4 \pm 1.44$ g, $p = 0.0061$). TRAMP animals held on a zinc-deficient diet were also significantly underweight compared to those fed a normal zinc diet and a zinc-supplemented diet; $W_{0.05\ ppm} = 26.9 \pm 2.85$ g vs. $W_{30\ ppm} = 30.1 \pm 3.08$ g ($p = 0.0199$) vs. $W_{150\ ppm} = 29.1 \pm 3.4$ g ($p = 0.0208$).

Dietary Zn effects on body weight, blood glucose (BG) management, and zinc bioavailability in health and prostate cancer

These data are reported as differential percentage (as outlined in Methods and in Fig. 2B) for WT and TRAMP animals that received GdL1, and either 2.2 mmol/kg glucose or saline as control. Both WT and TRAMP animals who received glucose exhibited no difference in BG after 10 min of exogenous glucose administration at any dietary zinc level. For the saline group, BG 10 min post GdL1 either remained unchanged in animals on a zinc deficient (0.05 ppm) ($-3.65 \pm 28.43\%$) or normal diet (30 ppm) ($-17.8 \pm 13.9\%$) but decreased significantly in animals fed a zinc supplemented (150 ppm) diet ($-27.1 \pm 14.4\%$, $p = 0.013$). This suggests that injection of GdL1 alone has an impact on BG when zinc is in excess.

Total serum zinc (as measured by ICP-MS) was relatively insensitive to levels of dietary zinc in WT and TRAMP animals and independent of glucose versus saline injection (Fig. 2C and Supplementary Fig. 1S). However, a slight trend emerges when comparing WT and TRAMP animals fed the same diet. For animals on a zinc-deficient diet, WT animals had significantly higher levels of serum zinc (23.33 ± 3.08 µM) compared to TRAMP animals (20.07 ± 3.01 µM, $p = 0.0148$). Conversely, in the same comparison for animals fed the high zinc diet, the TRAMP animals displayed a higher amount of serum Zn content (24.51 ± 5.13 µM) compared to WT animals (20.44 ± 2.11 µM, $p = 0.0081$). In animals fed a normal (30 ppm) zinc diet, serum zinc was identical in both WT and TRAMP animals (21.09 ± 3.98 µM vs. 22.38 ± 2.06 µM, $p = 0.4554$). These combined results suggest that WT animals respond to a zinc deficiency by increasing the bioavailability of zinc in serum while TRAMP animals lose their ability to do so (23.3 ± 3.08 µM vs. 20.4 ± 2.11 µM, $p = 0.0375$). Conversely, excess zinc is processed differently in healthy WT animals compared to TRAMP animals. In a state of zinc overload, healthy animals respond by decreasing the bioavailability of zinc in serum, while TRAMP animals have less capacity to normalize zinc levels.

The impact of dietary zinc on the distribution of zinc in prostate tissue by SR-XRF

Figure 3A shows a representative H&E section, XRF freeze-dried adjacent section, and XRF quantified image of prostate from a healthy control mouse fed a 0.05 ppm Zn diet. From H&E, the ventral, lateral, and dorsal lobes were delineated based on anatomical references as outlined in our previous work[21]. Here we can appreciate that the distribution of zinc differs between lobes where the lateral prostate lobe contains the highest zinc. Fig. 3B summarizes the elemental distribution of Zn, Gd, Cu, Fe, and Ca within each lobe as a function of dietary zinc in WT and TRAMP, raw concentration maps show the elemental distribution for both WT and TRAMP in Supplementary Figs. 4 and 5S, respectively. In general, zinc is consistently

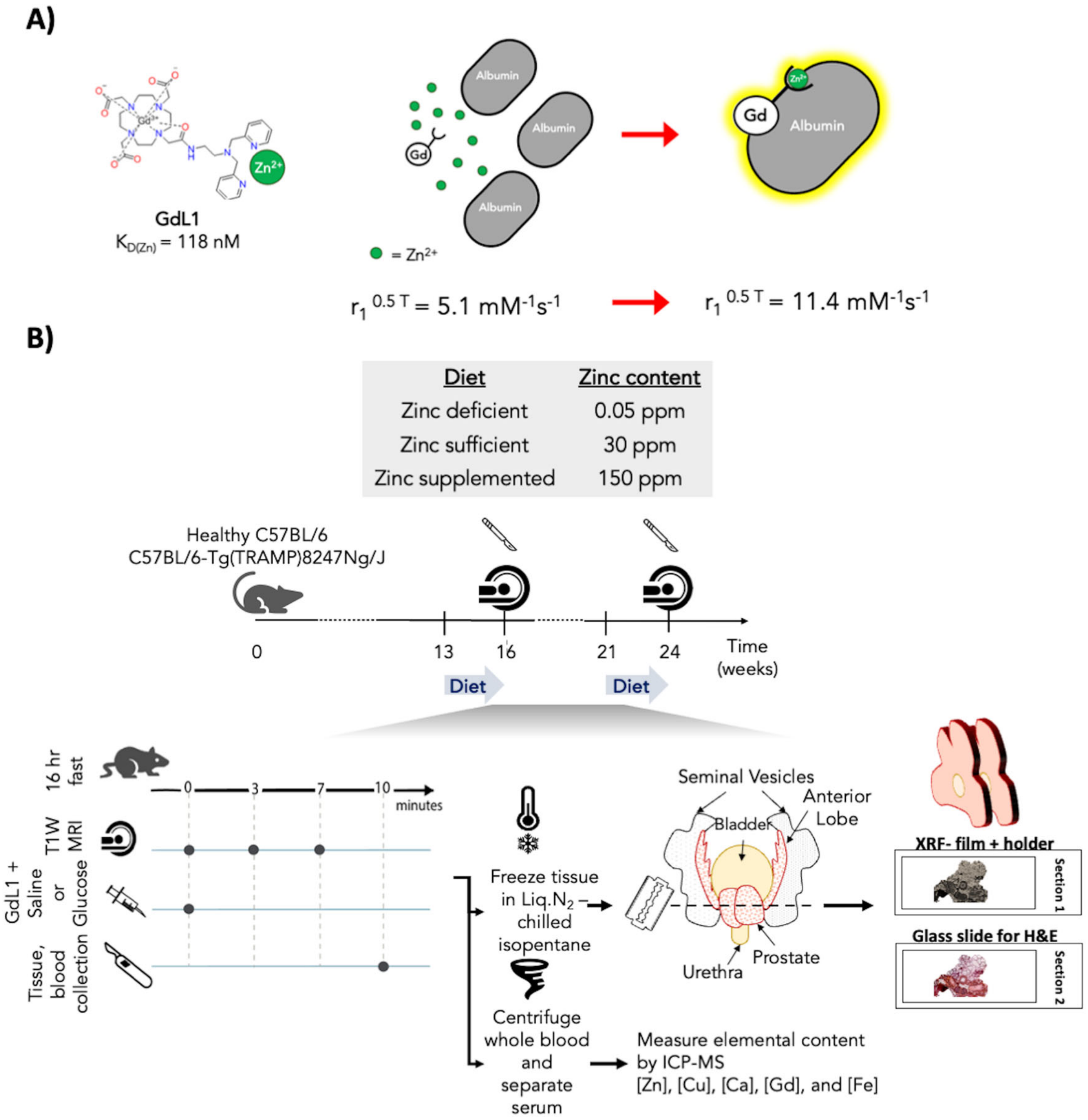

Fig. 1 | Study workflow and processing. **A** Schematic illustrating mechanism of zinc detection by MRI. **B** Study design including dietary regimen, imaging, sample collection and preparation for ex vivo analyses.

slightly higher in the lateral lobe of WT animals while Ca appears to be more concentrated in the ventral lobes (Fig. 3B). As shown in previous reports, Gd in tissue was detected after intravenous injection of a small Gd-based probe[21,24], here we found that the distribution of Gd in the three prostate lobes did not differ. Fig. 3C shows a comparison of zinc concentrations between the lateral *versus* ventral lobes. Here, although not statistically significant, the prostate of WT animals showed wide variations in zinc in the lateral lobes (±glucose) whereas the TRAMP lateral lobe did not show variations in zinc (±glucose). The ventral lobes in either the WT or TRAMP animals (±glucose) do not show this same trend consistent with the lateral lobe being largely involved in zinc storage and secretion.

The impact of dietary zinc on glucose-stimulated zinc secretion (GSZS) as measured by MRI

As demonstrated in several previous publications[16,21,25], a rapid increase in plasma glucose stimulates secretion of Zn^{2+} ions from the healthy prostate, and this is easily detected by the zinc-sensitive MRI contrast agent, GdL1. The XRF data described above show that variations in dietary zinc do not profoundly impact the amount of zinc stored in prostate tissue. Unlike XRF, which measures total tissue zinc, the MRI experiment only detects secretion of zinc ions from an intracellular storage depot into extracellular space, where it encounters GdL1. The images in Fig. 4A show that the WT prostate is nicely enhanced in all three groups of mice fed low, normal, and high levels of dietary zinc in response to an injection of glucose. The prostate images were also slightly enhanced when animals were injected with saline as a control, reflecting image enhancement simply due to the distribution of GdL1 in extracellular spaces. However, in animals injected with glucose to stimulate GSZS, even greater image enhancement over that produced by GdL1 alone was observed. In TRAMP mice, this difference was smaller because prostate image enhancement was significantly higher in saline control animals compared to that observed in WT mice. This reflects higher tissue vascularity of the TRAMP prostate[26]. To correct for differences in tissue vascularity, these data are presented as an "index of zinc efflux" (difference between saline and glucose images at 7 min after injection) for the three dietary groups in Fig. 4C. These data show clear differences in GSZS between animals fed low, normal, and high zinc diets in normal control animals. Interestingly, the TRAMP animals did not show similar trends in % zinc efflux from the prostate under these dietary changes. The TRAMP mouse prostate is known to lose its ability to regulate zinc storage[27] and as such may also lose

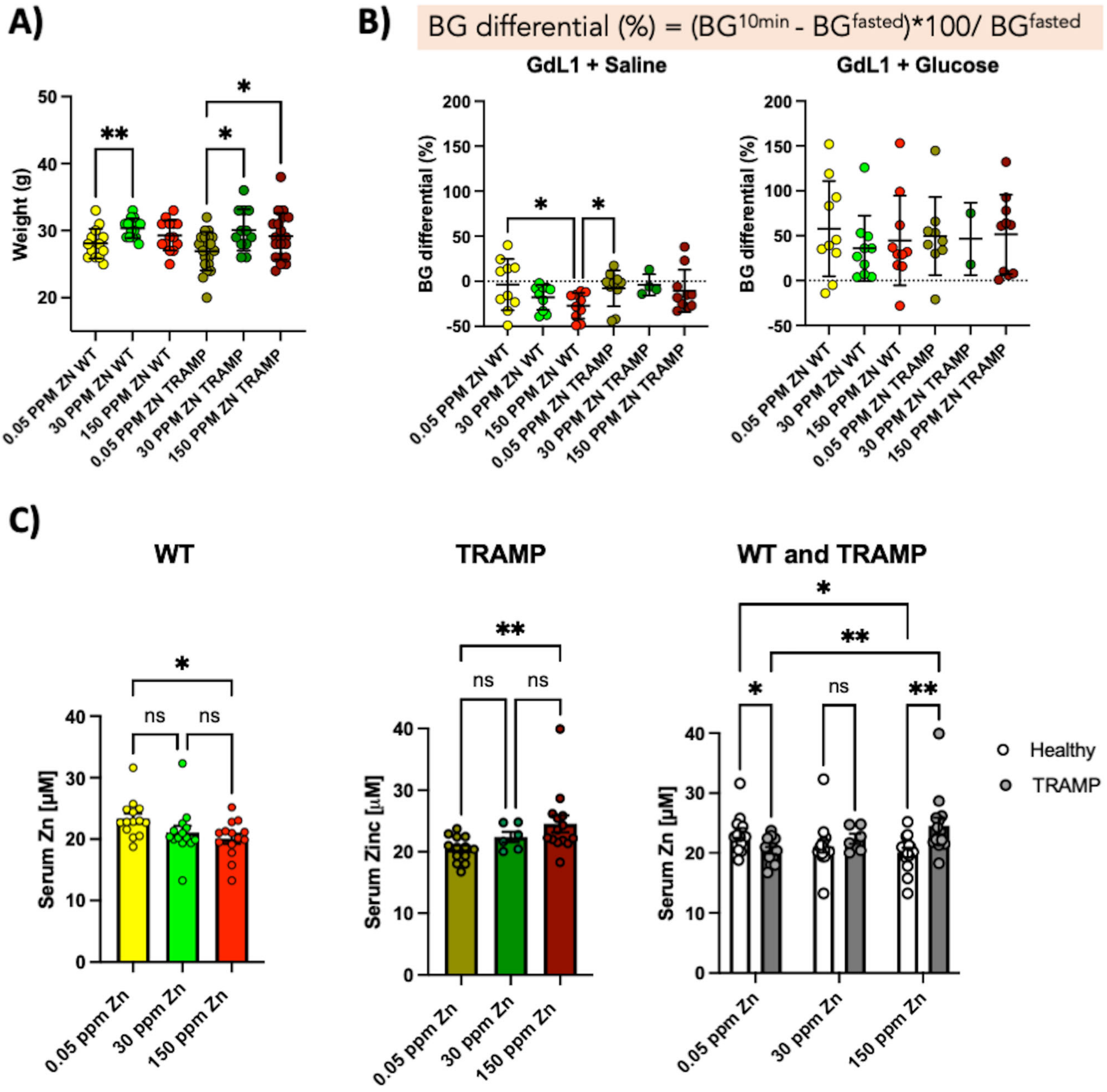

Fig. 2 | Dietary zinc affects weight, glucose management, and zinc bioavailability. **A** Mouse body weight measured after 21 days in variable Zn diet. **B** Blood glucose management expressed as a calculated change in blood glucose 10 min after receiving glucose or saline plus GdL1 by the equation shown. **C** Total zinc content in blood (ICP-MS) as a function of dietary Zn levels. The bar graph on the right summarizes statistical differences between WT and TRAMP animals. Data for all animals are included whether injected with glucose or with saline. Error Bars reflect SEM.

its ability to regulate secretion consistent with reduced GSZS and zinc efflux[22] as detected by MRI in these animals.

Discussion

The long-term goal of this research is to apply the GSZS imaging method in the general population of men undergoing diagnostic and surveillance scans for prostate malignancies. Given that zinc bioavailability could be influenced by dietary choices, this study was undertaken to evaluate the impact of dietary zinc content in the mouse prostate. Diets with the lowest zinc content include vegan, low-calorie, and high-fiber diets[28,29], while diets with the highest zinc content consists of high-protein, low-fiber, shellfish-rich diets[30]. The recommended daily zinc intake for adults is 8–11 mg daily, and vegans may require up to 50% more zinc than non-vegans due to the lower bioavailability of zinc in plant-based foods[31]. Therefore, the variability in zinc content based on dietary preferences across populations and cultures could potentially impact using MRI and GSZS to detect prostate cancer in man.

One of the central findings of this work is that a dietary zinc deficiency results in dysregulation of zinc both systemically and at the organ level. Zinc deficiency results in weight loss in both WT and TRAMP animals, supporting the idea that zinc deficiency results in anorexia and growth impairment, likely via leptin-mediated food regulation and intake[32]. In a state of zinc deficiency, the healthy mouse redistributes zinc in intracellular stores and results in higher levels of Zn in serum. Conversely, TRAMP animals fail to redistribute intracellular zinc stores and, as a result, maintain relatively deficient levels of zinc in serum. An intriguing result showed that GdL1 and saline resulted in further decrease in blood glucose suggesting a role for GdL1 in glucose homeostasis. This finding aligns with previous

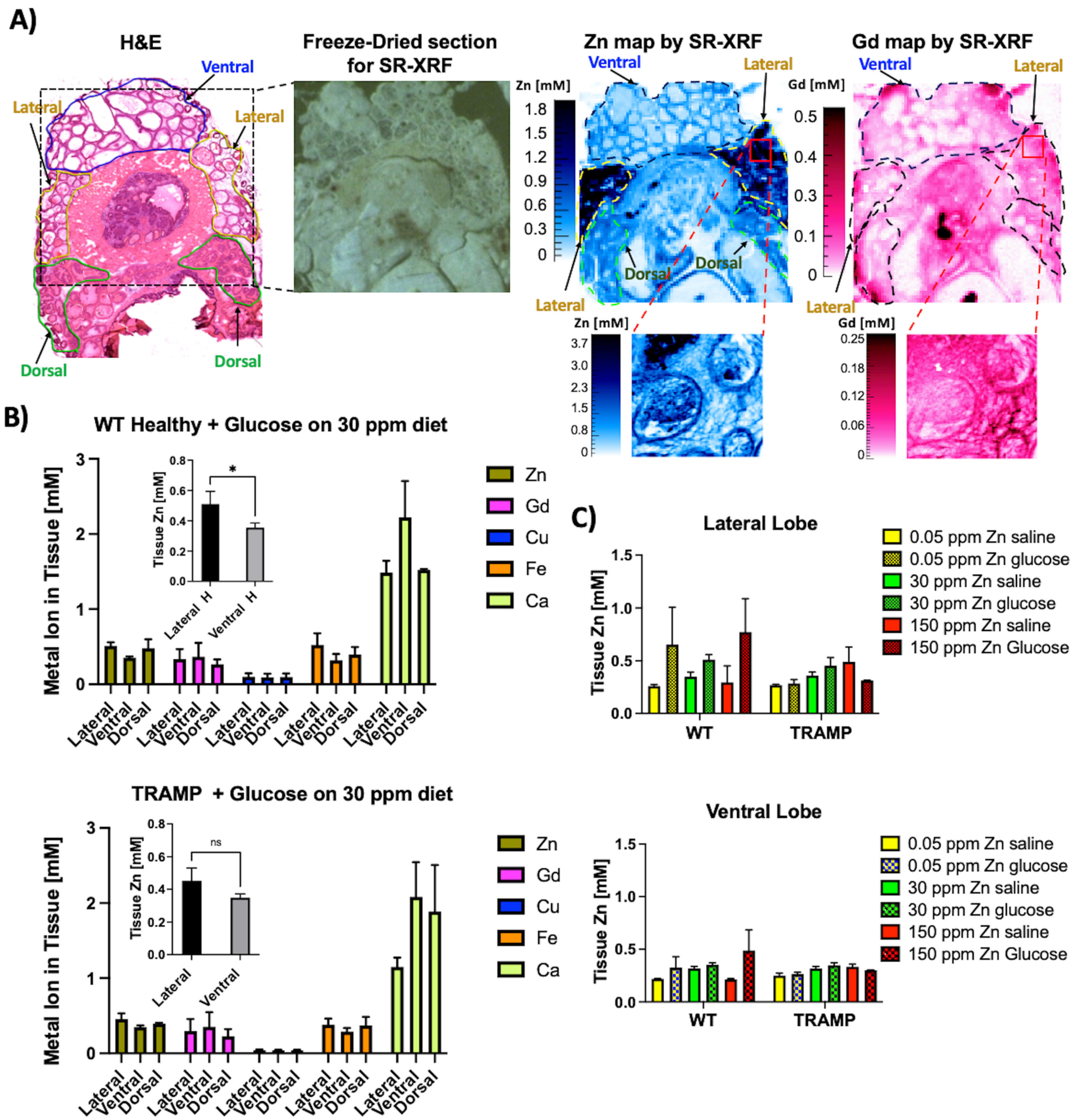

Fig. 3 | Elemental distribution in mouse healthy and prostate cancer tissue under variable zinc dietary conditions. A H&E and adjacent freeze-dried section for elemental mapping by SR-XRF. H&E slice illustrate the anatomical differences among the lobes, ROIs are drawn to identify the ventral lobe (blue), lateral lobe (yellow), and dorsal (green). Elemental map showing zinc and gadolinium distribution of WT receiving glucose showing distribution of zinc and gadolinium content within the gland. (insets) ROIs of lateral lobe illustrate the distribution of zinc and gadolinium relative to glandular and stromal compartments. Both Zn and Gd show overlap within glandular lumen and stromal spaces. **B** Representative Zn, Gd, Cu, Fe, and Ca distribution in the three distinct lobes of the prostate of WT receiving glucose (*N* = 3 for 30ppm diet) and TRAMP (*N* = 3 for 30ppm diet). **C** Zinc concentrations in lateral versus ventral lobes of WT (*N* = 3 for all diets and either glucose or saline) and TRAMP animals (*N* = 3 for all diets and saline, *N* = 3 for 30 ppm plus glucose, and *N* = 2 for 0.05 and 150 ppm Zn diet plus glucose) as a function of dietary zinc. Error bars reflect the SEM.

studies conducted in non-human primates where a Gd-based zinc probe (Gd-CP027) was infused into rhesus macaques and compared to Gadofosveset as a non-zinc sensitive control while co-administering a graded-glucose infusion. Blood measurements of insulin and c-peptide showed that Gd-CP027 potentiated insulin and c-peptide secretion when compared to Gadofosveset[33]. Therefore, we hypothesize that zinc may function as a second messenger, capable of transducing extracellular stimuli into intracellular signaling pathways. Although additional studies are required to fully elucidate this mechanism, we suggest that the release of zinc and insulin from beta cells modulates glucagon secretion via the uptake of zinc ions by neighboring alpha cells through zinc transporters. Given the high affinity of GdL1 for Zn ions, infusion or injection of this agent likely influences the activity of zinc transporters, which could potentially impact the signaling of glucagon secretion, thereby permitting unabated insulin secretion.

SR-XRF measurements showed a reduced zinc content in all prostate lobes in both WT and TRAMP fed a zinc-deficient diet. Interestingly, GSZS

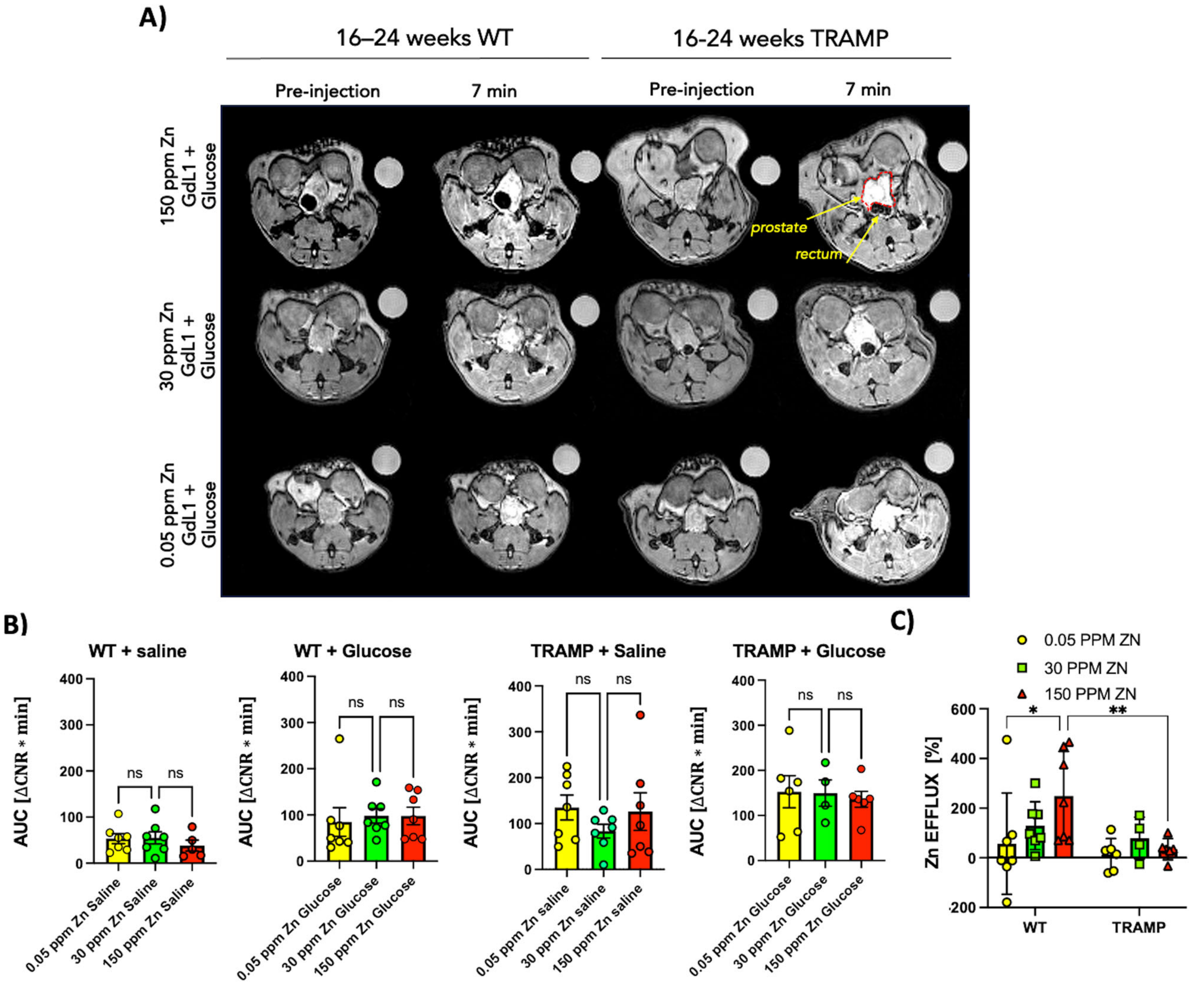

Fig. 4 | Glucose-stimulated zinc secretion MRI of the WT and TRAMP prostate under differential zinc dietary conditions. **A** T_1-weighted MRI pre- and post 0.07 mmol/Kg GdL1 and glucose for all three dietary levels in WT ($N = 7$ for all diets) and TRAMP animals (0.05 ppm Zn $N = 6$, 30 ppm Zn $N = 4$, and 150 ppm Zn $N = 6$). **B** Area under the CNR vs time curve capturing the overall signal in the prostate during the scanning period. WT + saline: 0.05 ppm Zn $N = 7$, 30 ppm Zn $N = 7$, and 150 ppm Zn $N = 5$, TRAMP + saline: $N = 7$ for all diets. **C** Calculated zinc efflux by normalizing the glucose stimulated signal in the prostate to unstimulated (saline) controls for WT and TRAMP. Error bars are SEM.

was evident by MRI in all WT animals regardless of diet while only a small increase in MRI signal enhancement was observed after glucose stimulation in TRAMP animals. However, after normalization by comparison of saline versus glucose injections in each dietary group, it became quite evident that GSZS increased in proportion to dietary zinc in the WT prostate, while GSZS in the TRAMP prostate showed overall reduced GSZS regardless of dietary zinc levels, consistent with a parallel between chronic zinc deficiency and malignant transformation. It has been postulated that the zinc-depleted aged rat prostate has a metabolic profile that resembles human prostate cancer, where there is a 10-fold down-regulation of citric acid, down-regulation of ZIP1, and overexpression of miR-183-96-182[32]. These factors increase cellular proliferation and a highly expressed COX-2 inflammatory phenotype, potentially establishing a link between prostatic zinc loss, citrate depletion, and prostate cancer[32].

Although the most dramatic effects were observed in the zinc-deficient groups, it does not indicate that a zinc-supplemented diet could be either protective or therapeutic for prostate cancer. In the current studies, zinc supplementation also resulted in aberrant regulation in the TRAMP prostate compared to WT, as reflected by the inability of TRAMP animals to regulate excess zinc in serum. The lower GSZS in TRAMP animals observed here is consistent with a previous report of a relationship between dietary zinc and prostate cancer in the TRAMP mouse[34]. In that report, the investigators provided a variable zinc diet (deficient, optimal, and high) to TRAMP animals and examined the impact of these dietary variables on prostate weight and carcinogenicity by performing serum measurements of insulin-like growth factor (IGF)-1 and binding protein 3 ratios. The investigators concluded that only optimal zinc had a protective role against cancer, while both zinc deficiency and excess zinc may have in turn deleterious effects on prostate health. Since the GSZS imaging method is intended to differentiate malignant lesions from normal prostate tissue and pathologically benign conditions, one may be able to take advantage of the inability to regulate an increase in zinc supply in prostate cancer. This means that under a zinc-supplemented diet, prostate cancer cells and tissue would not have the mechanisms in place to regulate the increase in supply, while the healthy prostate or pathologically benign prostate may be able to self-regulate by increasing its stimulated zinc efflux as observed here. This would increase malignant lesion conspicuity in a GSZS MRI scan.

The GSZS method for detection of prostate cancer (PCa) by MRI does have potential limitations. The fundamental basis for the GSZS method is that healthy prostate tissue has the capacity to accumulate and store more zinc than malignant prostate tissue so that when excess glucose is presented, it follows that more zinc should also be released from healthy prostate cells than from cancerous prostate cells and this difference should be detected as a difference in MR image intensity based upon greater activation of GdL1. In rodent models such as that described here, low molecular weight imaging agents such GdL1 are rather quickly excreted so one in principle should perform multiple imaging experiments in each animal where prostate image intensity is compared after injection of GdL1 plus saline versus GdL1 plus glucose. An additional control MR imaging experiment should also be done using non-zinc-responsive Gd-based agent with similar r_1 value, again plus or minus glucose. This second control experiment would account for differences in tissue vascularity of normal healthy prostate tissue versus malignant prostate tissue. This second set of control experiments were not performed in this study because our goal was simply to evaluate whether a higher level of dietary zinc has a major influence on GSZS as detected by MRI. Here, the greater vascularity of prostate tissue in the TRAMP model resulted in a higher MR signal intensity even in the absence of excess glucose so the MR intensity differences between ± glucose were small. Thus, a major limitation in rodent models is how to differentiate between tissues with higher vascularity versus tissues that release less zinc ions in response to a bolus of glucose. This limitation should in principle be much less restrictive for detecting PCa in man. First, low molecular agents like GdL1 are not cleared from tissues as rapidly as in mice. This means that a zinc-sensitive agent like GdL1 could be injected instead of a non-responsive Gd-based agent currently used in clinical multiparametric MRI studies while dynamic images are collected[35], followed by injection of a bolus of glucose and collection of a second image. In this case, additional MR image enhancement should only be detected in those tissue regions where a significant amount zinc was released in response to glucose. Hence, injection of a single zinc-responsive agent like GdL1 followed by collection of two T_1-weighted images may provide a direct index of zinc secretion in a single experiment. This GSZS technique has been successfully used to detect PCa in dogs with enlarged, highly vascular prostates[20].

We have demonstrated that TRAMP animals lose their ability to regulate extreme levels of dietary zinc, highlighting a dysregulation of zinc homeostasis in prostate cancer. We found that zinc deficiency impacts animal weight and systemic zinc bioavailability in healthy and TRAMP mice. This study also showed that Zn^{2+} is more readily released (initiated by glucose) from the healthy prostate in animals exposed to excess Zn^{2+} in their chow. These results suggest that dietary supplement of zinc prior to a GSZS study may enhance T_1-weighted contrast differences between malignant and non-malignant prostate tissue, thereby facilitating detection of prostate cancer by MRI in man.

Methods

Synthesis of GdL1

GdL1 was prepared and purified as described previously[13].

Variable zinc diet in WT and TRAMP animal models

Chow with variable zinc content was obtained from Dyets Inc. (Bethlehem, PA). Regular chow was used with a mineral mix withdrawn of zinc. The base chow was an egg white based AIN-93G diet with dextrose replacing sucrose to meet 1995 NRC requirements for growth. To formulate zinc-deficient, optimal, and excess diets, zinc was added in the following proportions: 0.05, 30, and 150 ppm. These formulations were DYET# 115400, 115437, and 115438, respectively. Wild-type and TRAMP animals were fed variable zinc chow ad libitum 21 days prior to imaging evaluation. Animals were housed in a temperature-controlled and light/dark (14 h/10 h) with access to water and chow ad libitum.

In vivo MRI

All animal experiments were performed according to guidelines approved by The University of Texas Southwestern Medical Center Institutional Animal Care and Use Committee. Male C57Bl6 mice were obtained from in-house breeding, and transgenic adenocarcinoma of the mouse prostate (TRAMP) mice were obtained from Jackson Laboratories at 6–8 weeks of age. Mice were provided the respective zinc-modified diet 21 days prior to imaging evaluation at 16, and 24 weeks of age. Mice were fasted overnight, weighed, and anaesthetized via inhalation of 1–5% isoflurane, prior to insertion of a tail-vein catheter. MR imaging was performed using 9.4 T Varian/Agilent scanner and a custom-built volume coil. Two baseline ge3d T1-weighted scans were obtained prior to injection of GdL1 (FA/TE/TR = 20°/1.756/3.476 ms, NEX 4, Matrix 128 × 128 × 128, FOV 30 × 30 mm). Mice then received 0.07 mmol/kg GdL1 via the tail-vein catheter, and an i.p. injection of either 2.2 mmol/kg glucose or saline as control. All agents were formulated to administer 2 $\mu l/g_{mouse}$ either i.p. or i.v. Immediately after injection, sequential 3D T_1-weighted scans were collected over 10 min. WT and TRAMP mice were euthanized by cervical dislocation under anesthesia after imaging to excise the entire prostate for synchrotron radiation X-Ray fluorescence analysis. Blood samples were obtained by tail vein puncture before and after MRI and glucose measurements were obtained using a hand-held glucometer. A region of interest (ROIs) covering the entire prostate but avoiding the urethra were used in evaluation of contrast-to-noise (CNR). The signal intensity (SI) of the prostate was subtracted from the signal intensity of an ROI of back muscle and divided by the standard deviation of an ROI placed outside the body capturing noise. $CNR = (SI^{prostate} – SI^{muscle}/St.dev^{air})$. A change in CNR ($\triangle$CNR) was then calculated by obtaining the difference between $CNR^{t\ (min)} – CNR^{baseline}$. The area under the $\triangle$CNR vs. time curve (AUC) was obtained for each animal using GraphPad Prism 10, (GraphPad Software, La Jolla, CA, USA).

Blood serum collection and elemental analysis by inductively-coupled plasma mass spectrometry (ICP-MS)

After each imaging study, animals were dissected, and the inferior vena cava was exposed. A 20 G needle was used to access the vein and collect whole blood. Blood was then left to coagulate for at least 30 min and then centrifuged for 10 min at 1000 × *g* at 4 °C, serum was separated, and the supernatant was stored at −80 °C until ICP-MS measurement. Samples were prepared by thawing at 30 °C, then placed in an ultrasonic water bath for 1 min and centrifuged at 4 °C for 10 min. Serum was collected from supernatant. Serum samples were digested in concentrated nitric acid (67%v/v) overnight and resuspended in 3 ml of diluent. Elemental analysis was then performed using an Agilent 8800-QQQ inductively coupled plasma-mass spectrometer (ICP-MS).

Histology and sample preparation

The mouse lower abdomen was shaven to prevent contamination from fur before dissection. The prostate was resected maintaining all lobes, urethra, and seminal vesicles intact. Once resected and rid of any adipose tissue, the prostates were slowly frozen by exposing them to liquid nitrogen-chilled isopentane. Briefly, a beaker was filled with isopentane and submerged in liquid nitrogen for 5 min. The liquid nitrogen level was slightly lower than that of isopentane. Once the prostate was resected, it was placed on a small weigh boat that allowed the prostate to float when directly placed on the chilled isopentane. Prostates remained on the floating weigh-boat for approximately 2–5 min, or until fully frozen. Samples were stored in sterile polypropylene 50-mL tubes at −80 °C until cryo-sectioning and transported on dry ice to avoid thawing. Blocks were surrounded by tissue tek compound optimal cutting temperature (OCT) gel and mounted flat, so that the area of interest was exposed for cutting. Several (two to four) 50-µm-thick cryosections (Cryo ultra microtome; Leica Microsystems, Richmond Hill, ON, Canada) were obtained per sample, interleaved by 20 µm-thick sections for hematoxylin and eosin (H&E) staining. Sections for XRF were mounted on custom-made slides, consisting of a thin sterile film for X-ray fluorescence (XRF) (3525 Ultralene from SPEX SamplePrep, NJ, Metuchen, USA) glued to a plastic holder. The 50-µm-thick-mounted sections were loaded into a freeze dryer (FreeZone 2.5; Labconco, Kansas City, MO, USA) pre-chilled to −50 °C and exposed to 0.7–1.5 mbar vacuum for 2–4 h. The 20 µm-thick sections mounted on glass slides were stained with H&E following standard histopathology protocols.

Micro-synchrotron radiation X-ray fluorescence (μSR XRF) imaging

μ-SRXRF is a non-destructive investigative technique that can determine the elemental composition and distribution of metals of interest. In this technique, a high intensity, monoenergetic synchrotron radiation beam is incident on a material, exciting the atom's electron structure and causing the emission of an x-ray characteristic of that atom. The energy of the emitted X-Ray is determined by the energy difference between the orbital shells the electron transitions to and from. As such, these characteristic X-Rays can be used to identify the presence of and, with proper calibration, the concentrations of different elements, with detection limits as low as a few parts per million. Samples were measured in air at the I18 Beamline at the Diamond Light Source, Harwell, United Kingdom. A 90∘ geometry was used such that samples placed on a translation stage are angled 45∘ to both the incident beam and the 4-element Vortex silicon drift detector (120 mm^2 active area). This geometry takes advantage of the strong polarization of the synchrotron beam to minimize noise from scattered photons. Initial scans of the whole sample are collected using a 50 μm × 50 μm beam size for a 0.75 s count time per pixel, at two energies of 8.2 and 11 keV to obtain accurate maps of P, S, Zn, Cu, Fe and Gd. These scans show sufficient anatomical detail to set a fine scan for a smaller region of interest. These smaller regions are approximately 300 μm × 300 μm and use a beam size of 5 μm × 5 μm for 1 s per pixel. The translational stage moves the sample in a raster scan pattern with a step size of 50 μm for coarse scans and 5 μm for fine scans.

μSR XRF elemental mapping

The spectra collected from raster scans are input into PyMCA X-Ray Fluorescence data analysis software (v5.6.3) for fitting and quantification. During fitting, a configuration file is created for the software to identify our material/matrix composition, subtract the background, identify elemental peaks of interest, separate overlapping peaks, and finally fit each peak to generate its intensity value. For quantification, PyMCA's internal libraries and code reference these intensity values with the measurements of a thin film standard reference material (AXO, Dresden) and calculated photon fluxes to generate a concentration value in parts per million (ppm). The sample and reference material were measured in the same experimental setup and conditions to ensure the quantification is accurate. The configuration is then used to batch fit each raster scan, generating the elemental composition for each pixel. Custom MATLAB® (R2022A) code and IDL software (v8.8), was used to arrange the PyMCA concentration data for each element of interest, and then generate element-specific maps. In IDL, regions of interest, for example specific prostate lobes or anatomical features, are identified by comparing the raster scans with the H&E-stained samples. The average concentration and standard error of the means for each region of interest are obtained in the IDL software and these statistics are compared to values obtained from other samples for analysis.

Statistical analyses

All statistical analyses were performed using GraphPad Prism 10, (GraphPad Software, La Jolla, CA, USA). Multiple statistical comparisons were performed by one-way ANOVA and post-hoc Tukey test correction for multiple comparisons. Comparisons between two groups were evaluated by two-tailed Student's t test. Statistical significance is annotated within the figures as $^{*}p < 0.05$, $^{**}p < 0.01$, $^{***}p < 0.001$, $^{****}p < 0.0001$.

Data availability

Data is provided within the manuscript or supplementary information files and raw data is available upon request to corresponding author.

Received: 4 June 2024; Accepted: 4 October 2024;

References

1. Maret, W. Zinc biochemistry: from a single zinc enzyme to a key element of life. *Adv. Nutr.* **4**, 82–91 (2013).
2. Kluska, K., Adamczyk, J. & Krężel, A. Metal binding properties, stability and reactivity of zinc fingers. *Coord. Chem. Rev.* **367**, 18–64 (2018).
3. Maret, W. & Vallee, B. L. Thiolate ligands in metallothionein confer redox activity on zinc clusters. *Proc. Natl Acad. Sci. USA* **95**, 3478–3482 (1998).
4. Sanna, A., Firinu, D., Zavattari, P. & Valera, P. Zinc Status and Autoimmunity: A Systematic Review and Meta-Analysis. *Nutrients* **10**, 68 (2018).
5. Fukada, T. & Kambe, T. Molecular and genetic features of zinc transporters in physiology and pathogenesis. *Metallomics* **3**, 662–674 (2011).
6. Lichten, L. A. & Cousins, R. J. Mammalian zinc transporters: nutritional and physiologic regulation. *Annu. Rev. Nutr.* **29**, 153–176 (2009).
7. Takagishi, T., Hara, T. & Fukada, T. Recent Advances in the Role of SLC39A/ZIP Zinc Transporters In Vivo. *Int. J. Mol. Sci.* **18**, 2708 (2017).
8. Fukunaka, A. & Fujitani, Y. Role of Zinc Homeostasis in the Pathogenesis of Diabetes and Obesity. *Int. J. Mol. Sci.* **19**, 476 (2018).
9. Gee, K. R., Zhou, Z.-L., Qian, W.-J. & Kennedy, R. Detection and Imaging of Zinc Secretion from Pancreatic β-Cells Using a New Fluorescent Zinc Indicator. *J. Am. Chem. Soc.* **124**, 776–778 (2002).
10. Chen, S. et al. In Vivo ZIMIR Imaging of Mouse Pancreatic Islet Cells Shows Oscillatory Insulin Secretion. *Front. Endocrinol.* **12**, 613964 (2021).
11. Li, D. et al. Imaging dynamic insulin release using a fluorescent zinc indicator for monitoring induced exocytotic release (ZIMIR). *Proc. Natl Acad. Sci. USA* **108**, 21063–21068 (2011).
12. Lubag, A. J., De Leon-Rodriguez, L. M., Burgess, S. C. & Sherry, A. D. Noninvasive MRI of β-cell function using a Zn2+-responsive contrast agent. *Proc. Natl Acad. Sci. USA* **108**, 18400–18405 (2011).
13. Martins, A. F. et al. Imaging Insulin Secretion from Mouse Pancreas by MRI Is Improved by Use of a Zinc-Responsive MRI Sensor with Lower Affinity for Zn(2+) Ions. *J. Am. Chem. Soc.* **140**, 17456–17464 (2018).
14. Thapa, B. et al. Imaging β-Cell Function Using a Zinc-Responsive MRI Contrast Agent May Identify First Responder Islets. *Front. Endocrinol.* **12**, 809867 (2022).
15. Yu, J. et al. Amplifying the Sensitivity of Zinc(II) Responsive MRI Contrast Agents by Altering Water Exchange Rates. *J. Am. Chem. Soc.* **137**, 14173–14179 (2015).
16. Clavijo Jordan, M. V. et al. Zinc-sensitive MRI contrast agent detects differential release of Zn(II) ions from the healthy vs. malignant mouse prostate. *Proc. Natl Acad. Sci. USA* **113**, E5464–E5471 (2016).
17. Costello, L. C. & Franklin, R. B. The clinical relevance of the metabolism of prostate cancer; zinc and tumor suppression: connecting the dots. *Mol. Cancer* **5**, 17 (2006).
18. Franklin, R. B., Milon, B., Feng, P. & Costello, L. C. Zinc and zinc transporters in normal prostate and the pathogenesis of prostate cancer. *Front. Biosci.* **10**, 2230–2239 (2005).
19. Costello, L. C. & Franklin, R. B. A comprehensive review of the role of zinc in normal prostate function and metabolism; and its implications in prostate cancer. *Arch. Biochem. Biophys.* **611**, 100–112 (2016).
20. Khalighinejad, P. et al. Magnetic Resonance Imaging Detection of Glucose-Stimulated Zinc Secretion in the Enlarged Dog Prostate as a Potential Method for Differentiating Prostate Cancer From Benign Prostatic Hyperplasia. *Investigative Radiol.* **56**, 450–457 (2021).
21. Clavijo Jordan, V. et al. Synchrotron Radiation X-ray Fluorescence Elemental Mapping in Healthy versus Malignant Prostate Tissues Provides New Insights into the Glucose-Stimulated Zinc Trafficking in the Prostate As Discovered by MRI. *Inorg. Chem.* **58**, 13654–13660 (2019).
22. Lo, S. T. et al. The Roles of ZnT1 and ZnT4 in Glucose-Stimulated Zinc Secretion in Prostate Epithelial Cells. *Mol. Imaging Biol.* **23**, 230–240 (2021).
23. Parrott, D. et al. Investigations into the signaling pathways involving glucose stimulated zinc secretion (GSZS) from prostate epithelial cells in vitro and in vivo. *Mol. Imaging Biol.* **25**, 935–943 (2023).

24. Le Fur, M. et al. Gadolinium-based Contrast Agent Biodistribution and Speciation in Rats. *Radiology* **309**, e230984 (2023).
25. Dao, E. et al. Using micro-synchrotron radiation x-ray fluorescence (micro-SRXRF) for trace metal imaging in the development of MRI contrast agents for prostate cancer imaging. *J. Trace Elem. Med. Biol.* **74**, 127054 (2022).
26. Wikström, P., Lindahl, C. & Bergh, A. Characterization of the autochthonous transgenic adenocarcinoma of the mouse prostate (TRAMP) as a model to study effects of castration therapy. *Prostate* **62**, 148–164 (2005).
27. Costello, L. C. et al. Human prostate cancer ZIP1/zinc/citrate genetic/metabolic relationship in the TRAMP prostate cancer animal model. *Cancer Biol. Ther.* **12**, 1078–1084 (2011).
28. Diethelm, K. et al. Nutrient intake of European adolescents: results of the HELENA (Healthy Lifestyle in Europe by Nutrition in Adolescence) Study. *Public Health Nutr.* **17**, 486–497 (2014).
29. Ferguson, E. L. et al. An interactive 24-h recall technique for assessing the adequacy of trace mineral intakes of rural Malawian women; its advantages and limitations. *Eur. J. Clin. Nutr.* **49**, 565–578 (1995).
30. G. International Zinc Nutrition Consultative. et al. International Zinc Nutrition Consultative Group (IZiNCG) technical document #1. Assessment of the risk of zinc deficiency in populations and options for its control. *Food Nutr. Bull.* **25**, S99–S203 (2004).
31. Hunt, J. R. Bioavailability of iron, zinc, and other trace minerals from vegetarian diets. *Am. J. Clin. Nutr.* **78**, 633S–639S (2003).
32. Fong, L. Y. et al. Human-like hyperplastic prostate with low ZIP1 induced solely by Zn deficiency in rats. *Proc. Natl Acad. Sci. USA* **115**, E11091–E11100 (2018).
33. Clavijo Jordan, V. et al. Imaging Beta-Cell Function in the Pancreas of Non-Human Primates Using a Zinc-Sensitive MRI Contrast Agent. *Front. Endocrinol.* **12**, 641722 (2021).
34. Prasad, A. S. et al. Dietary zinc and prostate cancer in the TRAMP mouse model. *J. Med. Food* **13**, 70–76 (2010).
35. Hotker, A. M., Vargas, H. A. & Donati, O. F. Abbreviated MR Protocols in Prostate MRI. *Life* **12**, 552 (2022).

Acknowledgements

The authors would like to acknowledge the following funding sources: CPRIT RP-180178, NIH/NCI K22CA241387, and National Institutes of Health (DK-095416). In addition, we are grateful for the advice and guidance from Dr. Peter Caravan.

Author contributions

V.C.J., A.D.S., and N.M.R. conceptualized the project. V.C.J., A.F.M., A.D.S. performed study design. V.C.J., A.F.M., P.K., and D.P. performed GSZS MRI. X.W., X.W., V.C.J., A.F.M., S.C. performed ex vivo and in vivo animal handling. P.G.G. performed serum ICP-MS analysis. E.D., K.G., M.F., V.C.J. performed SR-XRF. E.D., K.G., performed SR-XRF data analysis. V.C.J., performed MRI Data analysis. V.C.J., and A.D.S. drafted the main manuscript text. All authors contributed and reviewed the final version of the manuscript.

Competing interests

PATENTS: A) 10,207,013 B2*2/2019 Inventors: Christian Preihs, Jing Yi, V.C.J., Yunkou Wu, Khaled Nasr, A.D.S., S.C. B) 11,097,017 B2*8/2021 Inventors: Christian Preihs, Jing Yi, V.C.J., Yunkou Wu, Khaled Nasr, A.D.S., S.C. C) 11,713,305 B2*8/2023 Inventors: A.F.M., S.C., V.C.J., A.D.S. These patents pertain to the Gd-based zinc probe used in this manuscript. All three have been licensed by VitalQuan, LLC. INDIVIDUAL CONFLICT OF INTEREST: A.D.S. is a scientific C-Founder of VitalQuan, LLC and holds founders stock. The remaining authors declare no competing interests.

Additional information

Supplementary information The online version contains supplementary material available at https://doi.org/10.1038/s44303-024-00051-1.

Correspondence and requests for materials should be addressed to Veronica Clavijo Jordan.